

A multimessenger model for neutron star–black hole mergers

Gompertz, B p; Nicholl, M; Smith, J c; Harisankar, S; Pratten, G; Schmidt, P; Smith, G p

DOI:

[10.1093/mnras/stad2990](https://doi.org/10.1093/mnras/stad2990)

License:

Creative Commons: Attribution (CC BY)

Document Version

Publisher's PDF, also known as Version of record

Citation for published version (Harvard):

Gompertz, BP, Nicholl, M, Smith, JC, Harisankar, S, Pratten, G, Schmidt, P & Smith, GP 2023, 'A multimessenger model for neutron star–black hole mergers', *Monthly Notices of the Royal Astronomical Society*, vol. 526, no. 3, pp. 4585-4598. <https://doi.org/10.1093/mnras/stad2990>

[Link to publication on Research at Birmingham portal](#)

General rights

Unless a licence is specified above, all rights (including copyright and moral rights) in this document are retained by the authors and/or the copyright holders. The express permission of the copyright holder must be obtained for any use of this material other than for purposes permitted by law.

- Users may freely distribute the URL that is used to identify this publication.
- Users may download and/or print one copy of the publication from the University of Birmingham research portal for the purpose of private study or non-commercial research.
- User may use extracts from the document in line with the concept of 'fair dealing' under the Copyright, Designs and Patents Act 1988 (?)
- Users may not further distribute the material nor use it for the purposes of commercial gain.

Where a licence is displayed above, please note the terms and conditions of the licence govern your use of this document.

When citing, please reference the published version.

Take down policy

While the University of Birmingham exercises care and attention in making items available there are rare occasions when an item has been uploaded in error or has been deemed to be commercially or otherwise sensitive.

If you believe that this is the case for this document, please contact UBIRA@lists.bham.ac.uk providing details and we will remove access to the work immediately and investigate.

A multimessenger model for neutron star–black hole mergers

B. P. Gompertz¹,^{1,2}★ M. Nicholl¹,^{1,2,3} J. C. Smith,¹ S. Harisankar,¹ G. Pratten,^{1,2} P. Schmidt^{1,2} and G. P. Smith¹

¹*School of Physics and Astronomy, University of Birmingham, Birmingham B15 2TT, UK*

²*Institute for Gravitational Wave Astronomy, University of Birmingham, Birmingham B15 2TT, UK*

³*Astrophysics Research Centre, School of Mathematics and Physics, Queen's University Belfast, Belfast BT7 1NN, UK*

Accepted 2023 September 29. Received 2023 September 29; in original form 2023 May 12

ABSTRACT

We present a semi-analytic model for predicting kilonova light curves from the mergers of neutron stars with black holes (NSBH). The model is integrated into the MOSFIT platform, and can generate light curves from input binary properties and nuclear equation-of-state considerations, or incorporate measurements from gravitational wave (GW) detectors to perform multimessenger parameter estimation. The rapid framework enables the generation of NSBH kilonova distributions from binary populations, light curve predictions from GW data, and statistically meaningful comparisons with an equivalent binary neutron star (BNS) model in MOSFIT. We investigate a sample of kilonova candidates associated with cosmological short gamma-ray bursts, and demonstrate that they are broadly consistent with being driven by NSBH systems, though most have limited data. We also perform fits to the very well sampled GW170817, and show that the inability of an NSBH merger to produce lanthanide-poor ejecta results in a significant underestimate of the early ($\lesssim 2$ d) optical emission. Our model indicates that NSBH-driven kilonovae may peak up to a week after merger at optical wavelengths for some observer angles. This demonstrates the need for early coverage of emergent kilonovae in cases where the GW signal is either ambiguous or absent; they likely cannot be distinguished from BNS mergers by the light curves alone from ~ 2 d after the merger. We also discuss the detectability of our model kilonovae with the Vera C. Rubin Observatory's Legacy Survey of Space and Time (LSST).

Key words: software: data analysis – stars: black holes – (stars:) gamma-ray burst: general – stars: neutron – (transients:) black hole – neutron star mergers – (transients:) gamma-ray bursts.

1 INTRODUCTION

Our understanding of compact object mergers has made significant advances following the advent of gravitational wave (GW) astronomy, including the first ever detection in GW of a binary black hole (BBH) merger (Abbott et al. 2016), binary neutron star (BNS) merger (Abbott et al. 2017a), and most recently the merger of a neutron star–black hole (NSBH) system (Abbott et al. 2021c). Where neutron stars (NS) are involved, accompanying electromagnetic (EM) signals like short gamma-ray bursts (SGRBs; e.g. Paczynski 1986; Kouveliotou et al. 1993; Berger 2014) and kilonovae (Li & Paczyński 1998; Rosswog 2005; Metzger et al. 2010; Barnes & Kasen 2013; Metzger 2019) are expected. Both became confirmed counterparts of BNS mergers with the coincident detections of GW 170817 (Abbott et al. 2017a), GRB 170817A (Goldstein et al. 2017; Hallinan et al. 2017; Margutti et al. 2017, 2018; Savchenko et al. 2017; Troja et al. 2017, 2018b; D'Avanzo et al. 2018; Lyman et al. 2018; Mooley et al. 2018; Lamb et al. 2019a), and the kilonova AT2017gfo (Andreoni et al. 2017; Arcavi et al. 2017; Chornock et al. 2017; Coulter et al. 2017; Cowperthwaite et al. 2017; Drout et al. 2017; Evans et al. 2017; Lipunov et al. 2017; McCully et al. 2017; Pian et al. 2017; Shappee et al. 2017; Smartt et al. 2017; Soares-

Santos et al. 2017; Tanvir et al. 2017; Utsumi et al. 2017; Valenti et al. 2017; Villar et al. 2017; Kasliwal et al. 2017a; Nicholl et al. 2017a).

The association of kilonovae with BNS mergers has important implications for the production of heavy elements in the Universe. These thermal transients are powered by the radioactive decay of unstable heavy elements assembled by rapid neutron capture (r -process) nucleosynthesis following the merger (Lattimer & Schramm 1974; Eichler et al. 1989; Freiburghaus, Rosswog & Thielemann 1999). Modelling of the GW 170817 kilonova indicates that BNS mergers may be the dominant source of r -process elements in the Universe (Rosswog et al. 2018). However, comparisons with kilonova candidates associated with cosmological SGRBs (Berger, Fong & Chornock 2013; Tanvir et al. 2013; Jin et al. 2015, 2016, 2018, 2020; Yang et al. 2015; Kasliwal et al. 2017b; Troja et al. 2018a, 2019, 2022; Eyles et al. 2019; Lamb et al. 2019b; Fong et al. 2021; O'Connor et al. 2021; Rastinejad et al. 2022; Levan et al. 2023) imply that the yield of r -process elements is highly variable between events (Gompertz et al. 2018; Ascenzi et al. 2019; Rastinejad et al. 2021). In addition, significant uncertainties remain in the measured BNS merger rate. Estimates from GW events (320^{+490}_{-240} Gpc^{−3} yr^{−1}; Abbott et al. 2021b) are hampered by the low number of detections to date, while inferences from the rate of short GRB detections (270^{+1580}_{-180} Gpc^{−3} yr^{−1}; Fong et al. 2015) must account for the jet opening angle distribution, which is poorly constrained. The exact

★ E-mail: b.gompertz@bham.ac.uk

contribution BNS mergers make to the r -process census is therefore highly uncertain.

A growing number of studies seek to minimize this uncertainty through simultaneous modelling of both the EM and GW observations, where available (Margalit & Metzger 2017, 2019; Barbieri et al. 2019; Coughlin et al. 2019; Dietrich et al. 2020; Breschi et al. 2021; Nicholl et al. 2021; Raaijmakers et al. 2021). Measurements of the binary and post-merger remnant from GW interferometers like advanced Observatory (LIGO) (LIGO Scientific Collaboration 2015), advanced Virgo (Acernese et al. 2015), and KAGRA (KAGRA Collaboration 2019) can be combined with observations of the subsequent transient from EM observatories and synthesized into tighter posterior distributions for parameters that impact the nucleosynthesis yield (e.g. Abbott et al. 2017b). They can also provide more stringent constraints on the NS equation-of-state.

A significant additional uncertainty in the Universal r -process census is the contribution made by NSBH mergers (see e.g. Chen, Vitale & Foucart 2021). Such events are theoretically capable of driving SGRBs and kilonovae (e.g. Rosswog 2005; Tanaka et al. 2014; Paschalidis, Ruiz & Shapiro 2015; Desai, Metzger & Foucart 2019) if the NS is disrupted before plunging into the black hole (BH), and some candidate NSBH-driven events have been proposed in the literature (e.g. Troja et al. 2008; Yang et al. 2015; Jin et al. 2016; Kawaguchi et al. 2016; Gompertz, Levan & Tanvir 2020; Zhu et al. 2022). However, the mass of disrupted material that remains outside of the remnant BH event horizon is expected to be low if the mass ratio of the binary is high and/or the magnitude of the orbit-aligned component of the pre-merger BH spin is low or negative (Foucart et al. 2014; Pannarale & Ohme 2014; Kawaguchi et al. 2016; Foucart, Hinderer & Nissanke 2018). The early GW-detected NSBH merger events (Abbott et al. 2021c) and candidates (Abbott et al. 2021a; The LIGO Scientific Collaboration 2021a, b) exhibit total masses and mass ratios that are suitable for NS disruption. However, the measured BH spins are consistent with zero, and the mergers are not expected to be EM bright (Dichiara et al. 2021; Fragione 2021; Mandel & Smith 2021; Zhu et al. 2021; Gompertz et al. 2022). They appear to derive from the isolated binary evolution channel (Broekgaarden & Berger 2021; Broekgaarden et al. 2021), though potentially via a non-standard pathway (Gompertz et al. 2022). The exception is GW191219_163120 (The LIGO Scientific Collaboration 2021b), whose large mass ratio implies that the binary may have formed through dynamical capture (Gompertz et al. 2022).

While zero BH spin at the point of merger is a common prediction from population-synthesis modelling (e.g. for BBH systems; Qin et al. 2018; Fuller & Ma 2019), pathways to higher spin systems are possible through weak core–envelope coupling in BH progenitor stars, or tidal interactions following BH formation (Steinle & Kesden 2021; Steinle, Gompertz & Nicholl 2023). Should such systems be realized in nature, they are expected to be accompanied by bright kilonovae with nucleosynthesis yields up to 10x greater per event than that expected from BNS mergers (Tanaka et al. 2014). Their still-uncertain merger rate density may be comparable to that of BNS mergers, but could also be significantly lower (Mapelli & Giacobbo 2018; Eldridge, Stanway & Tang 2019; Belczynski et al. 2020; Abbott et al. 2021c). The potential contribution of NSBH mergers to Universal r -process production therefore ranges from none at all to being the dominant production sites of lanthanides and actinides through cosmic time. Calibrating their influence will require further detections of events in GW during LIGO–Virgo–KAGRA (LVK) observing runs to constrain merger rates,

as well as EM detections or stringent limits on emission that translates to meaningful measurements or constraints on r -process yields. This is best achieved through GW–EM multimessenger modelling.

In this paper, we present a semi-analytic forward model for NSBH-driven kilonovae that predicts light curves from the binary configuration and NS equation-of-state. The relative simplicity of our model compared to more simulation-based alternatives means that it is optimized for quickly generating light curves for arbitrary parameters, fitting to data, predicting populations, or marginalizing over unconstrained parameters. By providing the model within the MOSFIT framework (Guillochon et al. 2018), it is publicly available for easy use and adaptation, and trivial to perform model comparison against an equivalent BNS model (Nicholl et al. 2021), e.g. for modelling mass-gap systems, or when no GW data are available. In the absence of GW observations, fitting to kilonova light curves affords constraints on the properties of the progenitor binary. Any available GW information can be included in the priors to enable multimessenger inference of the merger, and tight constraints on the nucleosynthesis yield and equation of state.

Our paper is structured as follows. The model is described in Section 2 and compared to a well-sampled subset of SGRB kilonovae to see if any are compatible with being NSBHs in Section 3. We perform fits to the GW–EM multimessenger data set of GW170817 to search for a self-consistent NSBH solution in Section 4. We discuss the implications our model has for the detectability of NSBH kilonovae with the Vera C. Rubin Observatory in Section 5. Finally, we present our conclusions in Section 6. Magnitudes are in the AB system unless otherwise stated.

2 MODEL DESCRIPTION

A schematic overview of our model is shown in Fig. 1. For an EM transient to be produced, the NS must be disrupted by the tidal forces exerted upon it by the BH in the final stages of inspiral, with some mass remaining outside of the BH event horizon. Tidal disruption occurs if the NS overflows its Roche lobe at distances greater than the innermost stable circular orbit (ISCO) of the BH. This radius can be expressed as (cf. Bardeen, Press & Teukolsky 1972),

$$\hat{R}_{\text{ISCO}} = 3 + Z_2 - \text{sgn}(\chi_{\text{BH}}) \sqrt{(3 - Z_1)(3 + Z_1 + 2Z_2)}, \quad (1)$$

where $\hat{R}_{\text{ISCO}} = R_{\text{ISCO}}/M_{\text{BH}}$ is the normalized ISCO radius, M_{BH} is the BH mass, χ_{BH} is the orbit-aligned component of the BH's dimensionless spin parameter, $Z_1 = 1 + (1 - \chi_{\text{BH}}^2)^{1/3} [(1 + \chi_{\text{BH}})^{1/3} + (1 - \chi_{\text{BH}})^{1/3}]$, and $Z_2 = \sqrt{3\chi_{\text{BH}}^2 + Z_1^2}$.

An analytical fitting function for the mass of the material that remains outside of the BH event horizon was derived by Foucart et al. (2018). The fitting function was calibrated to 75 numerical relativity simulations (compiled from Etienne et al. 2009; Foucart et al. 2011, 2012, 2013, 2014; Kyutoku et al. 2011, 2015; Lovelace et al. 2013; Brege et al. 2018), and gives an ejected mass of

$$M_{\text{ej}} = M_{\text{NS}}^b \left[\max \left(\alpha \frac{1 - 2C_{\text{NS}}}{\eta^{1/3}} - \beta \hat{R}_{\text{ISCO}} \frac{C_{\text{NS}}}{\eta} + \gamma, 0 \right) \right]^\delta, \quad (2)$$

where the four fitting parameters were found to be $\alpha = 0.406$, $\beta = 0.139$, $\gamma = 0.255$, and $\delta = 1.761$. Equation (2) parametrizes the ejected mass in terms of \hat{R}_{ISCO} , $\eta = (1 + 1/q)^{-2} q^{-1}$ (where $q = M_{\text{NS}}/M_{\text{BH}}$ is the binary mass ratio), the compactness of the NS

$$C_{\text{NS}} = GM_{\text{NS}}/(R_{\text{NS}}c^2), \quad (3)$$

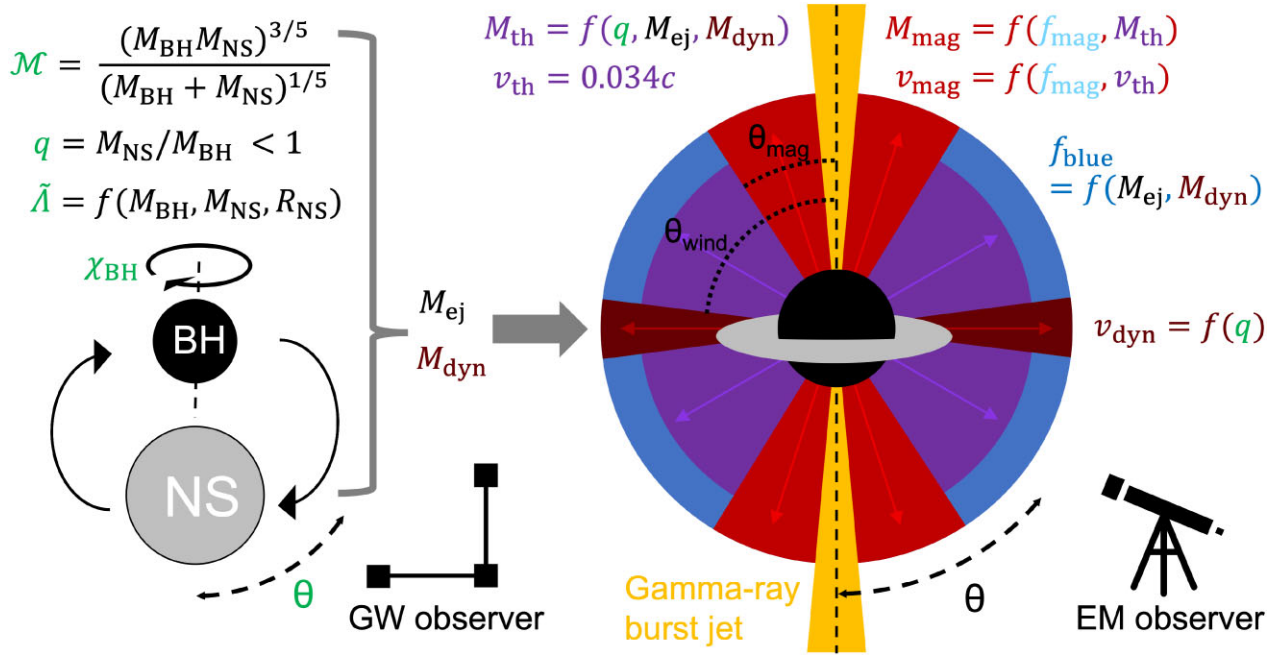


Figure 1. Schematic of the model. The five measured GW parameters are shown in green. The total ejecta mass [M_{ej} , equation (2); Foucart et al. 2018] and dynamical ejecta mass [M_{dyn} , equation (5); Krüger & Foucart 2020] are functions of the binary properties, and influence the kilonova light curve evolution. The masses and velocities of individual emission components are shown in their respective colours, along with their dependencies. The grey opacities for each component are $\kappa_{\text{blue}} = 1 \text{ cm}^2 \text{ g}^{-1}$, $\kappa_{\text{th}} = 5 \text{ cm}^2 \text{ g}^{-1}$, and $\kappa_{\text{mag}} = \kappa_{\text{dyn}} = 10 \text{ cm}^2 \text{ g}^{-1}$.

and its baryonic mass (cf. Lattimer & Prakash 2001),

$$M_{\text{NS}}^b = M_{\text{NS}} \left(1 + \frac{0.6 C_{\text{NS}}}{1 - 0.5 C_{\text{NS}}} \right). \quad (4)$$

The ejected mass of the merger is therefore primarily a function of the orbit-aligned component of the BH’s spin, the binary mass ratio, and the NS equation-of-state.

2.1 Dynamical ejecta

Krüger & Foucart (2020) developed an analytical fitting function for the mass of material ejected dynamically from an NSBH merger,

$$\frac{M_{\text{dyn}}}{M_{\text{NS}}^b} = a_1 q^{-n_1} \frac{1 - 2C_{\text{NS}}}{C_{\text{NS}}} - a_2 q^{-n_2} \frac{R_{\text{ISCO}}}{M_{\text{BH}}} + a_4. \quad (5)$$

The best-fitting parameters, validated against simulations by Kawaguchi et al. (2015) and Foucart et al. (2019), were found to be $a_1 = 0.007116$, $a_2 = 0.001436$, $a_4 = -0.02762$, $n_1 = 0.8636$, and $n_2 = 1.6840$. The average velocity of this ejecta was found to be an inverse function of q (Kawaguchi et al. 2016),

$$v_{\text{dyn}} = (0.01533q^{-1} + 0.1907)c. \quad (6)$$

The dynamical ejection of matter is primarily driven by tidal torque, and is therefore typically distributed within 10° – 20° of the orbital plane (e.g. Kawaguchi et al. 2015; Kyutoku et al. 2015). For simplicity we assume an axisymmetric distribution (see however Kyutoku et al. 2015; Kawaguchi et al. 2016). The tidal dynamical ejecta experience only weak neutrino irradiation (Kyutoku et al. 2018), meaning that the electron fraction is expected to be low ($Y_e \lesssim 0.1$; Foucart et al. 2014; Metzger & Fernández 2014; Kyutoku et al. 2018). We model the dynamical ejecta with a grey opacity of $\kappa_{\text{dyn}} = 10 \text{ cm}^2 \text{ g}^{-1}$ (Tanaka & Hotokezaka 2013; Kawaguchi et al. 2016; Kasen et al. 2017; Tanaka et al. 2020).

2.2 Disc winds

2.2.1 Thermally driven wind

Combining the work of Foucart et al. (2018) and Krüger & Foucart (2020), we obtain the disc mass,

$$M_{\text{disc}} = M_{\text{ej}} - M_{\text{dyn}}. \quad (7)$$

Hydrodynamic simulations show that some of the post-merger disc surrounding the remnant BH is driven away in neutron-rich winds by viscous heating and nuclear recombination (e.g. Fernández & Metzger 2013; Fernández et al. 2015; Just et al. 2015; Fernández, Foucart & Lippuner 2020; Fujibayashi et al. 2020). The fraction of the disc that is ejected this way was shown to be a linear function of the disc compactness by Fernández et al. (2020), and was parametrized as a function of the binary mass ratio by Raaijmakers et al. (2021) as

$$\xi = \frac{M_{\text{th}}}{M_{\text{disc}}} = \xi_1 + \frac{\xi_2 - \xi_1}{1 + e^{1.5(1/q-3)}}. \quad (8)$$

We assume $\xi_1 = 0.18$ and $\xi_2 = 0.29$, the median values given in Raaijmakers et al. (2021).

We combine equations (7) and (8) to obtain the mass of material driven from the disc by thermal pressure (M_{th}). This material is assumed to have an average velocity of $v_{\text{therm}} = 0.034c$ (Fernández et al. 2020). However, the outflow velocity is sensitive to the assumed viscosity parameter in the simulation, with higher viscous coefficients associated with more efficient acceleration of matter in the outer accretion disc (e.g. Fujibayashi et al. 2020).

The electron fraction of the thermal wind is typically found to be in the range $0.25 \leq Y_e \leq 0.35$ (e.g. Foucart et al. 2015; Fernández et al. 2020; Fujibayashi et al. 2020). This corresponds to a grey opacity of $\kappa \lesssim 5 \text{ cm}^2 \text{ g}^{-1}$ in Tanaka et al. (2020), with the true value tending towards the lower end of this range when temperatures are below

5000 K (e.g. $\kappa = 1 \text{ cm}^2 \text{ g}^{-1}$ in Kasen et al. 2017). Fernández et al. (2020) find that a significant portion of this wind has a lanthanide and actinide mass fraction $X_{(\text{La} + \text{Ac})} < 10^{-4}$. Motivated by this, we model the thermal wind as a two component mixture model featuring a leading blue edge with $\kappa = 1 \text{ cm}^2 \text{ g}^{-1}$ enveloping a redder core with $\kappa = 5 \text{ cm}^2 \text{ g}^{-1}$. The blue mass fraction (f_{blue}) was found to monotonically increase with disc mass by Fernández et al. (2020), so we calculate f_{blue} from M_{disc} (equation 7) using a first-order polynomial fit to the data in their table 2, noting the large scatter induced by varying the BH mass

$$f_{\text{blue}} = 0.20199 \log_{10}(M_{\text{disc}}) + 1.12692. \quad (9)$$

2.2.2 Magnetically driven wind

The inclusion of magnetic fields in three-dimensional general relativistic magnetohydrodynamic (GRMHD) models (Siegel & Metzger 2017, 2018; Christie et al. 2019; Fernández et al. 2019) has revealed a second outflow in the form of an MHD-mediated wind. This results in twice as much ejecta mass, a higher average ejecta velocity, and a lower average electron fraction (Y_e) when compared to equivalent hydrodynamic simulations (Fernández et al. 2019). The mass ejected by magnetic processes depends on the geometry of the post-merger magnetic field (Christie et al. 2019). More poloidal configurations eject more mass, and with higher velocities (cf. Fernández et al. 2019), while preferentially toroidal fields generate very little magnetically driven ejecta (cf. Siegel & Metzger 2018). Fernández et al. (2019) find that the magnetically driven outflow has a velocity $v > 0.1 c$, in excess of the maximum velocity seen in hydrodynamic simulations.

We include this second wind component in our fiducial model with the ignorance parameter f_{mag} , which accounts for the unknown magnetic field configuration. A fully poloidal field has $f_{\text{mag}} = 1$, while lower values represent more toroidal field geometries. It is applied as a fraction of the thermal wind ejecta mass derived in equation (8): $M_{\text{mag}} = f_{\text{mag}} M_{\text{th}}$, and as $v_{\text{mag}} = f_{\text{mag}} 0.22 c$, where $0.22 c$ is the average velocity of the faster bimodal component in the fully poloidal field geometry of Fernández et al. (2019). The velocity floor is set equal to the thermal wind velocity ($v_{\text{mag}} \geq 0.034 c$). The magnetic wind component has $Y_e \sim 0.1$, corresponding to $\kappa = 10 \text{ cm}^2 \text{ g}^{-1}$. This low electron fraction is maintained because the magnetic wind is driven from the disc towards the poles before it is significantly impacted by neutrino irradiation.

The inclusion of the magnetically driven wind means that our model predicts lanthanide rich and therefore optically faint emission. The assumption of high opacity and suppressed optical emission is common in semi-analytical models for NSBH kilonovae (e.g. Barbi-eri et al. 2019; Raaijmakers et al. 2021), where the lack of neutrino irradiation from a remnant NS means that the electron fraction is expected to be low. However, assuming neutrino irradiation from the inner accretion disc is sufficient to significantly raise the electron fraction can have a marked effect on the early optical light curve (e.g. Zhu et al. 2020).

2.3 Conversion to light curves

Our model calculates r -process ejecta masses and velocities from the input binary configuration. In order to convert them to kilonova light curves, we incorporate the NSBH ejecta model as a package in MOSFIT (Guillochon et al. 2018). r -Process masses and velocities are converted to light curves through pre-existing MOSFIT modules, including semi-analytical models for heating rates and deposition

(Korobkin et al. 2012; Barnes et al. 2016; Cowperthwaite et al. 2017; Villar et al. 2017; Metzger 2019), an approximation of photon diffusion through the ejecta (Arnett 1982), and self-consistent evolution of the photospheric radius (Nicholl, Guillochon & Berger 2017b).

The process to generate light curves is as follows (c.f. Villar et al. 2017): for each ejecta component, the radioactive heating rate with time is approximated (Korobkin et al. 2012) as:

$$L_{\text{in}} = 4 \times 10^{18} M_r \times \left[0.5 - \pi^{-1} \arctan \left(\frac{t - 1.3}{0.11} \right) \right]^{1.3} \text{ erg s}^{-1}, \quad (10)$$

where M_r is the mass of the r -process ejecta. This neglects any contribution from fallback accretion on to the remnant, which is expected to be prevented by winds from the disc (e.g. Fernández & Metzger 2013). Not all of this energy is available to power the kilonova because only a fraction ϵ_{th} thermalizes within the plasma. As the ejecta become more diffuse with time, the efficiency of thermalization decreases. This effect is approximated analytically (Barnes et al. 2016) as

$$\epsilon_{\text{th}}(t) = 0.36 \left[e^{-at} + \frac{\ln(1 + 2bt^d)}{2bt^d} \right], \quad (11)$$

where a , b , and d are constants that depend on the mass and velocity of the ejecta and are obtained by interpolating table 1 of Barnes et al. (2016).

Homologous expansion of the ejecta and central energy deposition are assumed, so that the observed bolometric luminosity of each ejecta component can be calculated as (Arnett 1982)

$$L_{\text{bol}}(t) = \exp \left(\frac{-t^2}{t_d^2} \right) \times \int_0^t L_{\text{in}}(t) \epsilon_{\text{th}}(t) \exp(t^2/t_d^2) \frac{t}{t_d} dt, \quad (12)$$

where $t_d \equiv \sqrt{2\kappa M_r / \beta v c}$ and $\beta = 13.4$ is a dimensionless constant. The spectral energy distribution (SED) of each component is calculated by assuming blackbody radiation with luminosity L_{bol} and a photospheric radius determined using the prescription in Nicholl et al. (2017b). The SEDs of individual emitting components are then summed in a ratio determined by their relative areas subtended to the observer (see Section 2.4), and transformed into light curves in individual photometric filters using the transmission curves available on the Spanish Virtual Observatory (SVO) filter profile service.¹

The assumptions built into the light curve creation add further systematic uncertainties to the model. First, the use of a grey opacity is a simplified approximation of the complex electron orbital transitions that are present in heavy elements like lanthanides and actinides. A full treatment of the (still incomplete) available atomic data (e.g. Smartt et al. 2017; Watson et al. 2019; Gillanders et al. 2022) may produce different evolution, especially at late times when the assumption of local thermal equilibrium breaks down (e.g. Hotokezaka et al. 2023; Levan et al. 2023; Gillanders et al. 2023a, b). Detailed nuclear heating with density-dependent thermalization has also been shown to introduce variability in the bolometric luminosity of kilonovae (Korobkin et al. 2021; Bulla 2023), which may impact parameter estimation from fitting. Finally, more detailed treatment of radiative transfer (e.g. Bulla 2019) will impact the light curve when compared to the simplified treatment of photon diffusion employed here.

¹<http://svo2.cab.inta-csic.es/theory/fps/>

Table 1. *Upper:* The free parameters of the NSBH kilonova model, their assumed fiducial values, and the prior ranges used when fitting. Bracketed values indicate a flat prior distribution, while Gaussian priors are given as median values with one sigma confidence intervals. The GW 170817 prior set uses the high spin priors from Abbott et al. (2017a). *Lower:* The masses and velocities produced by the fiducial model for each ejecta component (see Fig. 1).

Parameter	Fiducial value	Astrophysical prior	GW 170817 prior
\mathcal{M}^a (M_\odot)	2.22*	[1.0, 6.0]	$1.188^{+0.004}_{-0.002}$
q^b	0.28*	[0.1, 1.0]	[0.4, 1.0]
$\tilde{\Lambda}^c$	11.0*	[0.0, 100.0]	[0.0, 700.0]
χ_{BH}^d	0.8	[-1.0, 1.0]	[-0.01, 0.17]
$\cos \theta^e$	0.707	[0.0, 1.0]	[0.883, 1.0]
$\cos \theta_{\text{mag}}^f$	0.707	[0.5, 1.0]	[0.5, 1.0]
$\cos \theta_{\text{wind}}^g$	0.174	[0.0, 0.342]	[0.0, 0.342]
f_{mag}^h	1.0	[0.1, 1.0]	[0.1, 1.0]
$\log N_H^i$	19.0	[19.0, 23.0]	[19.0, 23.0]
Parameter	Fiducial value		
M_{dyn}	$0.047 M_\odot$		
M_{mag}	$0.036 M_\odot$		
M_{th}	$0.036 M_\odot$		
v_{dyn}	0.25 c		
v_{mag}	0.22 c		
v_{th}	0.034 c		

Notes. ^aChirp mass. ^bMass ratio. ^cEffective tidal deformability of the binary. ^dOrbit-aligned component of the BH spin. ^eObserver viewing angle. ^fOpening angle of the magnetic wind. ^gOpening angle of the wind–dynamical ejecta boundary. ^hMagnetic wind fraction. ⁱHydrogen column density in host galaxy (proportional to extinction). *These parameters describe a binary with a $5 M_\odot$ BH and a $1.4 M_\odot$ NS with a 12 km radius.

2.4 Geometry

The outflow geometry is structured in a similar fashion to Nicholl et al. (2021). We assume an axially symmetric kilonova and model each emission component as a cutout with a conical polar cap defined in terms of its half-opening angle θ_{open} . Emitting regions are constructed following the formalism of Darbha & Kasen (2020), where the luminosity of each region is scaled to the area of the caps projected to an observer at a viewing angle θ_{obs} . See their appendix A for the mathematical expressions. For fiducial parameters we assume that the magnetic wind is restricted to polar regions with $\theta_{\text{mag}} = 45^\circ$, the thermal wind occupies moderate latitudes ($\theta_{\text{wind}} = 80^\circ$) and the dynamical ejecta sits $\pm 10^\circ$ from the equator. A schematic of the model is shown in Fig. 1. We note that the evolution of the projected area of the photosphere is complicated in the presence of multiple emission components, especially when they are likely non-spherical (e.g. Zhu et al. 2020; Just et al. 2022).

For simplicity, our model assumes that the emitting regions do not interact. This is a reasonable assumption for the tidally ejected dynamical component, but interactions between the thermal and magnetic winds are likely to produce turbulence along their contact interface. However, our assumption is a reasonable approximation for the majority of viewing angles, and the 50:50 contribution of the two emitting regions when viewed along the boundary between them is also likely a reasonable proxy for a mixed emission component. We do not account for the possibility of polar cavities carved out by a relativistic jet launched by the merger, which may expose hot, low opacity material (Klion et al. 2021; Nativi et al. 2021).

One caveat to our model is that it is based on simulations where the BH spin axis and binary orbital axis are aligned. It has been shown that only considering the aligned spin cases still results in accurate

estimates of the mass that remains outside of the BH (Foucart et al. 2013; Kawaguchi et al. 2015). However, misalignment may induce spin precession, which breaks symmetry and is likely to result in asymmetric structure in the ejecta (e.g. Kawaguchi et al. 2015). This is not captured in our model.

2.5 Connecting to compact binary coalescences

The shape of the kilonova light curve is underpinned by the properties of the merging binary, which can be measured from GW observations. The most accurately measured GW parameter is the ‘chirp’ mass (\mathcal{M}), which is related to the binary component masses by $\mathcal{M} = (M_{\text{BH}} M_{\text{NS}})^{3/5} (M_{\text{BH}} + M_{\text{NS}})^{-1/5}$. GW measurements can also provide constraints on the viewing angle θ , the mass ratio q , and the orbit-aligned BH dimensionless spin χ_{BH} .

One parameter of particular importance when estimating the mass of material that remains outside of the event horizon [equation (2)] is the NS compactness, C_{NS} . When fitting combined GW–EM multimessenger data, C_{NS} can be measured rather than assumed, leading to constraints on the NS equation-of-state. From the EM side, C_{NS} can be constrained via the best-fitting ejecta mass from the kilonova light curve. The signal detected by GW detectors is a mass-weighted combination of the tidal deformability of the two binary components, known as the effective tidal deformability ($\tilde{\Lambda}$; Flanagan & Hinderer 2008; Wade et al. 2014; Raithel, Özel & Psaltis 2018). Tidal deformability is a measure of the responsiveness of a body to an external tidal field, and is zero for a BH (Binnington & Poisson 2009; Damour & Nagar 2009). In the NSBH case, the tidal deformability of the NS can therefore be calculated from the component masses of the binary and the effective tidal deformability,

$$\Lambda_{\text{NS}} = \frac{13}{16} \frac{\tilde{\Lambda} (M_{\text{BH}} + M_{\text{NS}})^5}{(M_{\text{NS}} + 12 M_{\text{BH}}) M_{\text{NS}}^4}. \quad (13)$$

We then relate this quantity to C_{NS} using the quasi-universal relation derived in Yagi & Yunes (2017),

$$C_{\text{NS}} = 0.360 - 0.0355 \ln(\Lambda_{\text{NS}}) + 0.000705 \ln(\Lambda_{\text{NS}})^2. \quad (14)$$

Our final model consists of nine free parameters. These are listed in Table 1 with their fiducial values and assumed priors. The GW and EM branches of the model and the relationship between the measured and derived parameters is shown in Fig. 1.

2.6 Parameter sensitivity

Fig. 2 shows how the kilonova light curves are affected by varying χ_{BH} , the binary mass ratio (by changing M_{BH}), the observer angle, and the assumed dipole field configuration through f_{mag} . As expected, higher BH spins and more symmetric binary mass ratios produce brighter kilonovae in all observing filters because they lead to a greater ejected mass outside of the remnant event horizon. We find that the *K*-band brightness is largely insensitive to viewing angle, likely due to the highly similar colour, mass, and velocity of the dynamical ejecta at the equator and the magnetically driven wind at the poles in our fiducial model. The bluer bands are more sensitive to the viewing angle, with the *g*-band light curves appearing ~ 1.5 mag brighter at peak for an equatorial observer than a polar one at 3–5 d after merger. This is because an equatorial viewing angle provides the widest range of sight lines to the thermal wind of the three viewing angles presented, and hence the largest relative contribution from the lowest opacity material to the received flux. This finding suggests that NSBH-driven kilonovae may peak quite strongly in the optical up to a week after merger for oblique viewing angles, in stark contrast to

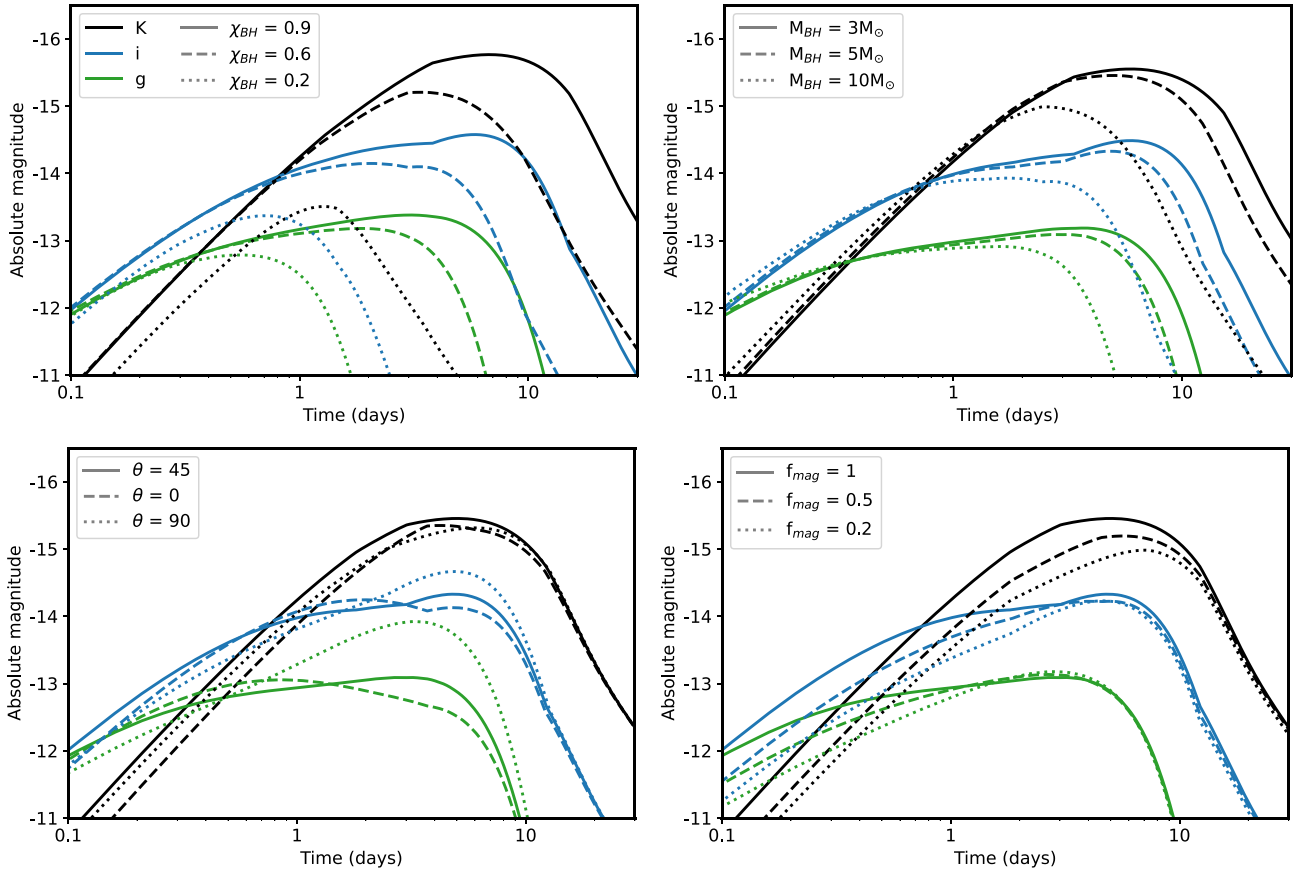


Figure 2. Example light curves in the K (black), i (blue), and g (green) bands for our fiducial model (Table 1), with variations in a single parameter per panel. *Top left:* varying χ_{BH} , the orbit-aligned BH spin. *Top right:* varying q , the binary mass ratio (via M_{BH}). *Bottom left:* varying θ , the observer inclination from the pole. *Bottom right:* varying f_{mag} , the magnetic field geometry.

BNS events. However, significant neutrino irradiation from the inner accretion disc or preferential photon diffusion towards the poles may result in an earlier optical peak and a reversal in the observer angle dependence (e.g. Kawaguchi, Shibata & Tanaka 2020; Zhu et al. 2020). Finally, we find that varying the magnetic field geometry has a moderate (~ 1 mag) effect on the peak brightness in the K band, due to the larger mass ejection associated with more polar field geometries (i.e. increasing f_{mag}). A similar effect is seen in the early ($\lesssim 1$ d) optical evolution, where higher velocity magnetic winds lower the density of the ejecta more rapidly, allowing photons to escape to the observer sooner.

3 COMPARISON TO GRB-KILONOVAE

In this section, we compare a selection of kilonova candidates associated with cosmological SGRBs to our fiducial model (see Table 1). Fig. 3 shows the light curves of five afterglow + kilonova candidates. These include the first reported GRB-kilonova candidate (GRB 130603B; Berger et al. 2013; Tanvir et al. 2013), the two best-sampled GRB-kilonovae outside of GW 170817 (GRB 160821B and GRB 211211A; Troja et al. 2019, 2022; Lamb et al. 2019b; Rastinejad et al. 2022; Gompertz et al. 2023), and two examples of kilonova candidates alongside ‘extended emission’ (EE; Norris & Bonnell 2006; Norris, Gehrels & Scargle 2010; Gompertz et al. 2013) SGRBs (GRB 050709 and GRB 060614; Jin et al. 2015, 2016; Yang et al. 2015). EE SGRBs have been suggested as candidates for NSBH-

driven events (Troja et al. 2008; Gompertz et al. 2020), and exhibit ~ 100 s of rapidly evolving high energy emission (Gompertz et al. 2023) in addition to the $\lesssim 2$ s prompt spike. In each case, our fiducial model is combined with power-law or broken power-law profiles that approximate the GRB afterglow. The parameters used are shown in Table 2.

The comparisons are deliberately approximate; in many cases the available data is not sufficient to constrain the large number of parameters needed to model both the GRB afterglow and the kilonova. Nevertheless, we demonstrate that even without fine tuning, our fiducial NSBH kilonova model provides rough agreement with the candidate kilonova excesses seen in SGRBs. Our fiducial NSBH kilonova model (Table 1) produces $0.05 M_{\odot}$ of dynamical ejecta (red equatorial ejecta; $\kappa_{\text{dyn}} = 10 \text{ cm}^2 \text{ g}^{-1}$) with a mean velocity of $0.25 c$. It also produces $0.04 M_{\odot}$ of magnetically driven wind ejecta (red polar ejecta; $\kappa_{\text{mag}} = 10 \text{ cm}^2 \text{ g}^{-1}$) with a mean velocity of $0.22 c$, and $0.04 M_{\odot}$ of thermally driven wind ejecta (‘purple’ ejecta; $\kappa_{\text{mag}} = 5 \text{ cm}^2 \text{ g}^{-1}$) with a mean velocity of $0.034 c$. We compare this to the r -process masses inferred using other published model fits in the literature for each GRB.

3.1 GRB 050709

GRB 050709 was detected by the *High Energy Transient Explorer 2* (HETE-2; Lamb et al. 2000). It featured a short, hard prompt spike with $t_{90} = 70 \pm 10$ ms in the 30–400 keV energy band, followed by

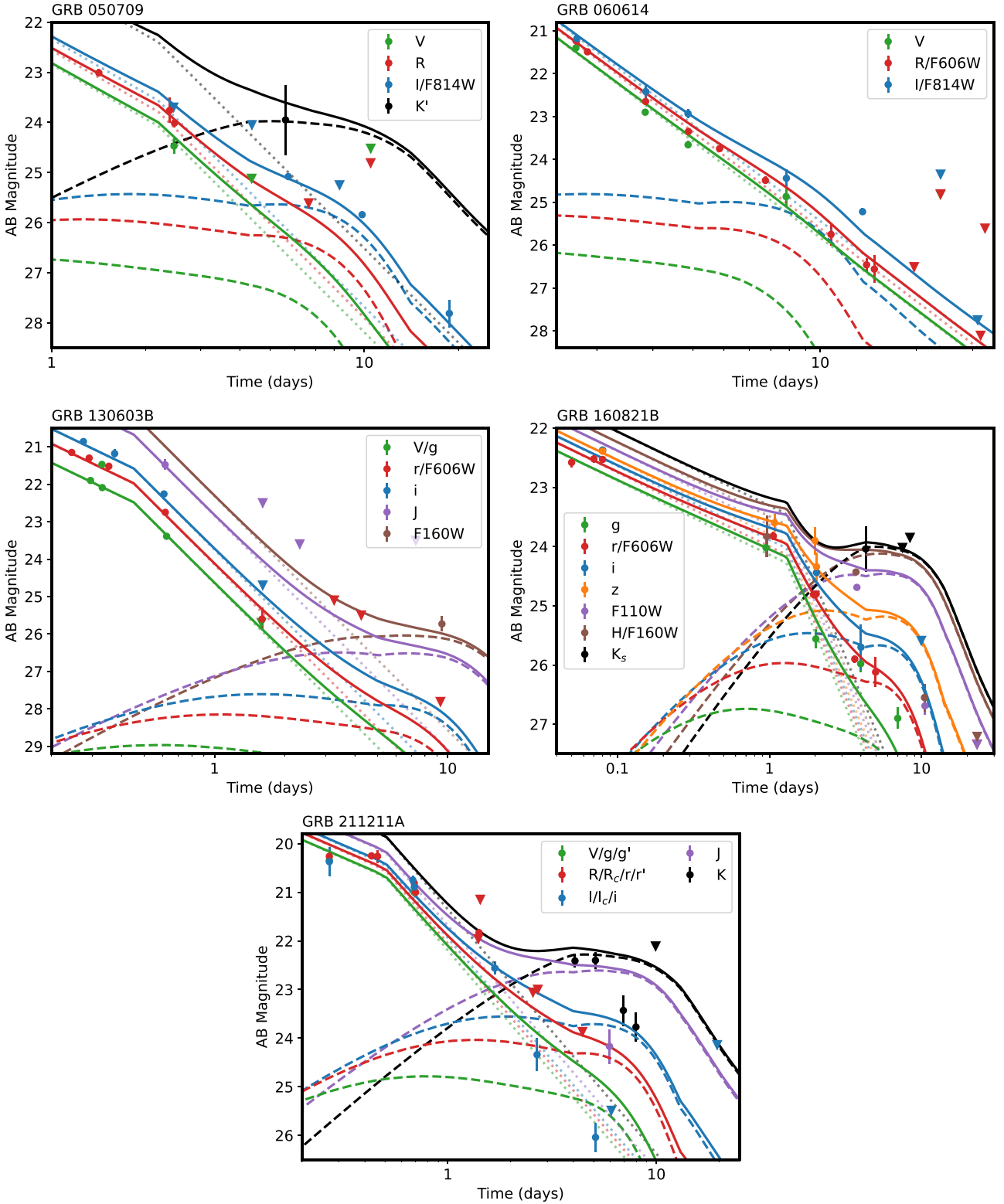


Figure 3. Model comparison to five kilonova candidates associated with cosmological GRBs. Our fiducial NSBH kilonova model (dashed lines, see Table 1) is scaled to the distance of each GRB and assumes a polar viewing angle ($\cos \theta = 1$). The GRB afterglow is approximated by power-law or broken power-law profiles with flux $F \propto t^{-\alpha} \nu^{-\beta}$ (dotted lines). Solid lines show the sum of the two components. Note that the kilonova models are not fit to the data in any way.

Table 2. The luminosity distance (d_L) of the five GRBs in Fig. 3 with the spectral (β) and temporal (α) indices and break times (t_b) used to approximate their afterglows.

GRB	d_L (Mpc)	β	α_1	t_b (d)	α_2
050709	795	1.0	1.4	2.2	2.5
060614	608	0.8	2.3	–	–
130603B	1960	1.8	1.2	0.5	2.5
160821B	806	0.5	0.5	1.3	2.5
211211A	350	0.5	0.8	0.5	2.0

a long-soft tail with $t_{90} = 130 \pm 7$ s in the 2–25 keV energy band (Villasenor et al. 2005), where t_{90} is the time in which the middle 90 per cent of event photons are collected. GRB 050709 is therefore an EE SGRB. It was the first SGRB for which an optical counterpart was identified (Hjorth et al. 2005) and was associated with a galaxy at $z = 0.16$ (Fox et al. 2005). A kilonova was first claimed in GRB 050709 by Jin et al. (2016). Photometry was taken from Fox et al. (2005), Covino et al. (2006), and Jin et al. (2016). We find that the Jin et al. (2016) $I_{\text{Vega}} = 24.1 \pm 0.2$ detection at $t \sim 2.5$ d is incompatible with the contemporaneous g - and r -band detections and preceding r -band detection under an afterglow interpretation, and use the $I_{\text{Vega}} > 23.25$ upper limit from Covino et al. (2006) for this epoch.

Our fiducial model provides a good qualitative match to the data. This is in agreement with Jin et al. (2016), who found best-fitting with an ejecta mass of $0.05 M_{\odot}$ and a velocity of $0.2 c$ from an NSBH merger, consistent with the fiducial model. However, we note that all of the data can be adequately described by a GRB afterglow model if the jet break occurs at $t \sim 10$ d, and hence the veracity of the GRB 050709 kilonova candidate remains uncertain.

3.2 GRB 060614

GRB 060614 was detected by the *Burst Alert Telescope* (BAT; Barthelmy et al. 2005) on board the *Neil Gehrels Swift Observatory* (Gehrels et al. 2004). The burst duration of $t_{90} = 102$ s (15–350 keV; Gehrels et al. 2006) is significantly above the canonical $t_{90} = 2$ s divide between short and long GRBs (Kouveliotou et al. 1993). However, at a redshift of $z = 0.125$ (Della Valle et al. 2006; Gal-Yam et al. 2006), deep optical observations exclude an associated supernova to limits hundreds of times fainter than the archetypal GRB supernova SN1998bw (Della Valle et al. 2006; Fynbo et al. 2006; Gal-Yam et al. 2006). GRB 060614 is therefore most likely a merger-driven EE SGRB (see however, Cobb et al. 2006), further supported by its negligible spectral lag (Gehrels et al. 2006) and strong spectral evolution (Mangano et al. 2007). Based on its light curve, Yang et al. (2015) and Jin et al. (2015) claimed evidence for a kilonova counterpart. Photometry was taken from Della Valle et al. (2006), Yang et al. (2015), and Gal-Yam et al. (2006).

The emission of GRB 060614 is likely dominated by the bright afterglow at almost all epochs; a deviation from a power law is only detected in two points (Yang et al. 2015). Our fiducial model provides a reasonable approximation of the i -band excess at ≈ 8 d, but underpredicts the flux in the ≈ 13 d epoch. Fine tuning to produce a slightly fainter and longer-lived kilonova signature may resolve the discrepancy, which can be achieved with e.g. a lower velocity wind. Yang et al. (2015) suggest an NSBH merger with kilonova ejecta mass of $\approx 0.1 M_{\odot}$ and velocity $\approx 0.2 c$, with an effective temperature of ≈ 2000 K. This is broadly consistent with the fiducial model, which produces $\approx 0.07 M_{\odot}$ of ejecta combined between

the magnetic and thermal winds, at a temperature of 2500 K and $v_{\text{mag}} = 0.22 c$.

3.3 GRB 130603B

GRB 130603B was detected by *Swift*–BAT with a duration of $t_{90} = 0.18 \pm 0.02$ s (15–350 keV; Lien et al. 2016) and is therefore an unequivocal member of the SGRB class. With a redshift of $z = 0.356$ (Cucchiara et al. 2013; Thone et al. 2013), it is also the most distant GRB in our comparison sample. GRB 130603B was the first ever identified kilonova candidate (Berger et al. 2013; Tanvir et al. 2013) thanks to a significant excess in HST F160W over the expected afterglow, constrained by a simultaneous HST F606W non-detection. Photometry was taken from Tanvir et al. (2013).

The fiducial model provides a good match to the data, although the kilonova is only detected in a single epoch and hence the observations are not particularly constraining. Kawaguchi et al. (2016) showed that GRB 130603B can be described with an NSBH-driven kilonova model for reasonably high spins ($\chi_{\text{BH}} > 0.3$) and larger NS radii. Berger et al. (2013) find that the light curve can be described by a kilonova driven by either a BNS or BHNS with an ejecta mass of 0.03 – $0.08 M_{\odot}$ and a velocity in the range of 0.1 – $0.3 c$, consistent with our fiducial model. Tanvir et al. (2013) find a similar mass range: $10^{-3} < M_{\text{ej}} < 10^{-2} M_{\odot}$.

3.4 GRB 160821B

GRB 160821B was detected by *Swift*–BAT with $t_{90} = 0.48 \pm 0.07$ s (15–350 keV; Lien et al. 2016). The kilonova was reported independently by Lamb et al. (2019b) and Troja et al. (2019), with the redshift found to be $z = 0.16$. Multiwavelength observations, particularly those at X-ray and radio frequencies, suggested that GRB 160821B afterglow may have experienced late energy injection from a second blast wave arriving at the afterglow emission site at late times (Lamb et al. 2019b). Such a phenomenon is not captured in our simple power-law representation of the afterglow. We use the photometry from Kasliwal et al. (2017b) and Lamb et al. (2019b).

Despite higher sampling than most of the other GRBs presented in this work, the fiducial model does remarkably well in matching the evolution of GRB 160821B with no fine-tuning of the kilonova. We note that the J - and H -bands are overpredicted, particularly at late times, implying that the mass of the reddest ejecta needs to be reduced or its emission evolve faster. This can be achieved with a lower binary mass ratio or BH spin. We also underpredict the emission in the g -band, which may indicate a lower grey opacity or higher blue ejecta fraction (from the thermal wind) is needed. Lamb et al. (2019b) find a good fit to the data with a refreshed afterglow and a two-component kilonova model with a wind ejecta mass of $0.01 M_{\odot}$ travelling at $v < 0.15 c$ and a dynamical ejecta mass of $0.001 M_{\odot}$ with $v > 0.1 c$. Troja et al. (2019) find a low, lanthanide-rich ($\kappa = 10 \text{ cm}^2 \text{ g}^{-1}$) ejecta mass of $\lesssim 0.006 M_{\odot}$ and $v \gtrsim 0.05 c$. The low ejecta masses inferred by both studies are as much as an order of magnitude less than is produced in our fiducial model, and may explain why it overpredicts the late near-infrared evolution.

3.5 GRB 211211A

GRB 211211A was detected by the *Fermi* Gamma-ray Burst Monitor (GBM; Meegan et al. 2009) and *Swift*–BAT, with the latter measuring $t_{90} = 51.4 \pm 0.8$ s (15–350 keV; Stamatikos et al. 2021). The burst is therefore an EE SGRB (for a full analysis of the high-energy emission see Gompertz et al. 2023). At a redshift of $z = 0.076$ (Rastinejad et al.

2022), GRB 211211A is the second-closest compact binary merger to Earth ever discovered, with only the GW-localized GW170817 more proximal. The kilonova was identified through a strong infrared excess by Rastinejad et al. (2022) and was independently modelled by Mei et al. (2022), Troja et al. (2022), Xiao et al. (2022), Yang et al. (2022), and Zhu et al. (2022). We use the photometry from Rastinejad et al. (2022).

Similar to GRB 160821B, our fiducial model struggles to evolve fast enough to reproduce the late near-infrared observations. It overpredicts the flux at essentially all wavelengths beyond ~ 2 d, particularly in the i -band (though we note that these suffer from significant systematic errors in their magnitude measurements; Rastinejad et al. 2022). Rastinejad et al. (2022) find best-fitting kilonova model with a total ejecta mass of $0.047^{+0.026}_{-0.011} M_{\odot}$, half of which is partitioned in a lanthanide-rich ‘red’ component with $v \approx 0.3$ c. The other half is divided equally between an intermediate-opacity ‘purple’ component with $v \approx 0.1$ c and a lanthanide-free ‘blue’ component with $v \approx 0.3$ c. A BNS merger was preferred over an NSBH. The total ejecta mass is lower than is produced by the fiducial model. The relative abundance of lanthanide-rich, high velocity ejecta could be achieved with a strong magnetic wind in our model, implying a high magnetic field with poloidal geometry. A strong dipole field is inferred for GRB 211211A by Gao, Lei & Zhu (2022).

Mei et al. (2022) fit the observations with an isotropic, one-component kilonova model. They find an ejecta mass of $0.020^{+0.009}_{-0.006} M_{\odot}$ with an average velocity of $0.10^{+0.07}_{-0.04}$ c, and a grey opacity of $0.6^{+0.8}_{-0.3} \text{ cm}^2 \text{ g}^{-1}$. Troja et al. (2022) find that the observations can be matched with $0.01\text{--}0.1 M_{\odot}$ of wind ejecta and $0.01\text{--}0.03 M_{\odot}$ of dynamical ejecta from a BNS merger. Zhu et al. (2022) employ an NSBH binary-driven model, and find the observations are best described by the merger of a $8.21^{+0.77}_{-0.75} M_{\odot}$ BH with dimensionless spin $0.62^{+0.06}_{-0.07}$ with a $1.23^{+0.06}_{-0.07} M_{\odot}$ NS, producing $0.005\text{--}0.03 M_{\odot}$ of lanthanide-poor wind ejecta and $0.015\text{--}0.025 M_{\odot}$ of lanthanide-rich dynamical ejecta. Finally, Yang et al. (2022) find a lanthanide-poor kilonova ($\kappa = 0.8^{+0.1}_{-0.2} \text{ cm}^2 \text{ g}^{-1}$) with a total ejecta mass of $0.027^{+0.011}_{-0.001} M_{\odot}$ at an average velocity of $0.25^{+0.06}_{-0.02}$ c.

4 FITTING TO GW 170817

There is only one GW–EM multimessenger data set available for fitting: that of GW 170817 (Abbott et al. 2017b). Observational and modelling evidence strongly supports this event being a BNS merger, but some parameter space is available for NSBH models with BH masses below typical expectations. Coughlin & Dietrich (2019) showed that an NSBH merger could potentially reproduce the GW and EM constraints, but is disfavoured relative to a BNS merger.

In this section, we investigate the ability of our model to reproduce the GW signal and kilonova associated with GW 170817. We approach this in two different ways. In the first approach, we use an ‘astrophysical’ prior that does not include the posteriors derived from GW 170817, and instead allows the model to explore the full parameter space for NSBH mergers that are expected to be EM bright while penalizing realizations that lie outside of theoretical expectations. Specifically, we penalize solutions with NSs more massive than the maximum stable NS mass (the Tolman–Oppenheimer–Volkoff mass, M_{TOV} , e.g. Shapiro & Teukolsky 1986), which we set as $M_{\text{TOV}} = 2.17$ (Margalit & Metzger 2017; Nicholl et al. 2021), as well as BHs with masses below this threshold. We also penalize solutions with tidal deformabilities outside of the expected range (e.g. Hinderer 2008; Hinderer et al. 2010; Postnikov, Prakash & Lattimer 2010). The second approach takes the posterior solutions

from Abbott et al. (2017a) as the model priors, but relaxes the penalties for unconventional solutions. The first formalism therefore allows the model to search for a more ‘canonical’ NSBH binary system that best reproduces the light curve, and the second challenges it to find a solution that satisfies the GW signal even where it defies expectations.

Fitting is performed with EMCEE (Foreman-Mackey et al. 2013). Our best-fitting solutions for the two prior sets are shown in Fig. 4. While the model provides a reasonably good match to the late emission and redder bands, it significantly underproduces the early optical emission. This result is expected; even BNS models, which are capable of providing more ‘blue’ emission than the NSBH case, require additional means for producing optical light when modelling GW 170817 and other well-sampled kilonovae (Nicholl et al. 2021; Rastinejad et al. 2022). Whether additional emissive mechanisms such as the shock heating of ejecta by a GRB jet (e.g. Kasliwal et al. 2017a; Arcavi 2018; Piro & Kollmeier 2018) can be included in NSBH models depends on whether sufficient polar material is present prior to the launching of the jet (if one is launched at all by NSBH mergers), and will require GW–EM observations to confirm. It is notable that beyond ~ 2 d, it becomes very difficult to distinguish the light curves of kilonovae driven by BNSs and NSBHs, and hence early observations are essential where the GW signal is either absent or ambiguous.

The posteriors for the astrophysical prior show a loose preference for a chirp mass of $\mathcal{M} = 3.01^{+0.70}_{-0.56}$, a mass ratio of $q = 0.11^{+0.03}_{-0.00}$, and an effective tidal deformability of $\tilde{\Lambda} = 0.91^{+0.88}_{-0.23}$. This translates into $M_{\text{BH}} \approx 11.6 M_{\odot}$, $M_{\text{NS}} \approx 1.3 M_{\odot}$, and $R_{\text{NS}} \approx 12.1$ km. The BH spin is preferentially high, at $\chi_{\text{BH}} = 0.82^{+0.04}_{-0.05}$. The viewing angle is equatorial, $\cos \theta = 0.07^{+0.09}_{-0.06}$, and the magnetic field geometry is strongly dipolar at $f_{\text{mag}} = 0.94^{+0.05}_{-0.21}$. Broadly, these parameters maximize the ejected mass while retaining sight lines to the bluer material.

The event-based priors limit the posterior solutions to within 28° of the poles (Abbott et al. 2017a), leading to a polar solution with $\cos \theta = 1.00^{+0.00}_{-0.01}$, in contrast to the results from the less restrictive astrophysical prior set. The preferred chirp mass is $\mathcal{M} = 1.19^{+0.00}_{-0.00}$, strongly constrained by the tight Gaussian priors from the GW detection. The binary mass ratio is found to be $q = 0.41^{+0.01}_{-0.01}$, with an effective tidal deformability of $\tilde{\Lambda} = 122.1^{+16.0}_{-9.1}$. These properties define a binary with $M_{\text{BH}} \approx 2.2 M_{\odot}$, $M_{\text{NS}} \approx 0.9 M_{\odot}$, and $R_{\text{NS}} \approx 9.7$ km.

The low component masses for the event-based priors are dictated by the tight constraints on the chirp mass from GW 170817. This has a knock-on effect of requiring a small NS radius to avoid overproducing the emission; the NS tidal deformability is already ~ 1500 with $R_{\text{NS}} \approx 9.7$ km. However, this combination of low NS mass and radius would point to very stiff equations of state. The BH is found to have a relatively low orbit-aligned spin magnitude, with $\chi_{\text{BH}} = 0.15^{+0.02}_{-0.04}$, again mandated by the GW priors. As with the astrophysical prior set, the magnetic field geometry is preferentially dipolar (the configuration that produces the most ejecta mass, and hence luminosity), with $f_{\text{mag}} = 0.99^{+0.01}_{-0.04}$. While the binary solutions are notably different between the two prior sets, the resultant kilonovae are strikingly similar (Fig. 4). These results suggest that the biggest discriminant of merger type comes from the bluer bands, where bright emission from high Y_e dynamical ejecta driven from the poles is produced at early times ($\lesssim 2$ d) in the BNS model but not in our NSBH model. However, blue emission may be produced in the polar outflows of an NSBH merger if the neutrino flux from the remnant disc can raise the electron fraction of the ejecta sufficiently (e.g. Zhu et al. 2020), or if photons preferentially diffuse to polar

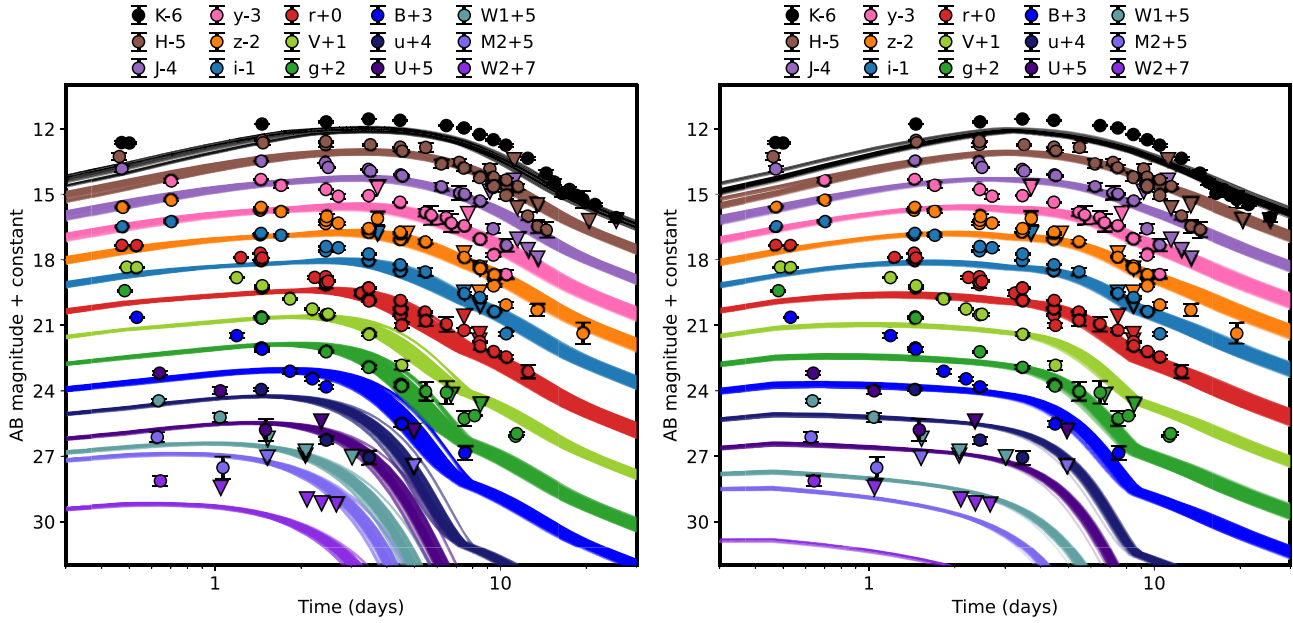


Figure 4. Light curves from the posterior distributions of the best-fits to the GW 170817 data (Villar et al. 2017) using the NSBH kilonova model and the general astrophysical priors (left) or event-based GW 170817 priors (right). The model provides a reasonable match to the data at times later than 2 d after trigger, but struggles to produce the early emission in both cases, particularly in optical and ultraviolet bands.

regions due to high equatorial opacities (e.g. Kawaguchi et al. 2020). Concurrent optical and nIR monitoring will be essential to distinguish between these possibilities.

5 DETECTABILITY WITH RUBIN

With its wide field of view and large aperture, the Vera C. Rubin Observatory (Rubin) will be well-suited to discovering EM counterparts to GW triggers (e.g. Andreoni et al. 2022) and serendipitous transients during its Legacy Survey of Space and Time (LSST; Ivezić et al. 2019). We investigate the detectability of the population of NSBH kilonovae predicted by our model by drawing 2000 light curve realizations from our model in generative mode. This mode enables the user to define their priors in terms of component mass and NS radius rather than chirp mass and deformability, and hence is suitable for simulating populations or fitting when no GW data are available. In particular, it helps to avoid realizations with unrealistic NS masses, which are hard to mitigate against when defining populations with chirp mass and mass ratio. BH and NS mass prior distributions were constructed following model C in Broekgaarden et al. (2021), and the NS radius was set to 11 km, following Nicholl et al. (2021). We generate our population out to 600 Mpc from Earth, which covers the full NSBH detection range predicted for advanced LIGO in O5 (Abbott et al. 2020). Priors for the other parameters were taken from the astrophysical set (Table 1), but negative χ_{BH} was excluded.

Of the 2000 realizations, 727 produce detectable emission, 1273 are EM dark, and 8 were discarded for numerical artefacts in their light curves. Histograms of the peak magnitudes of our realizations in different bands are shown in Fig. 5. Assuming a detection threshold of $g = 24.81$ and $i = 23.92$ for LSST’s Wide Fast Deep (WFD) survey (Ivezić et al. 2019), we obtain 279 g -band detections and 237 i -band detections. Assuming a GW follow-up strategy that reaches a depth of $g = 26$ and $i = 25$ (Andreoni et al. 2022), this becomes 655 g -band detections and 599 i -band detections. However, we define

‘detections’ as realizations with peak magnitudes above the detection threshold. In reality, it is unlikely these transients would be recovered from faint detections in single epochs. We also do not account for line-of-sight extinction and the cadence of follow-up observations. These estimates of the fraction of realizations that are detectable should therefore be considered upper limits.

Our model therefore predicts that less than one-third of NSBH GW triggers (assuming a maximum distance of 600 Mpc from Earth) will yield EM detections with LSST even if all are well sampled by follow-up observations. Sampling the whole localization region on each of the first four nights following a GW trigger, as per the *preferred* strategy of Andreoni et al. (2022), would achieve sufficient coverage. By contrast, the reduced depth of the WFD survey compared to GW follow-up observations makes it significantly less likely that our model kilonovae would be serendipitously discovered. Only ~ 10 per cent of realizations would be detectable if observed by chance at peak magnitude.

By way of comparison, we also investigate the detectability of a population of 2000 BNS mergers, using the model of Nicholl et al. (2021). NS mass and mass ratio priors are chosen to be Gaussian and are taken from the sample of Galactic BNS systems presented in Farrow, Zhu & Thrane (2019). We limit our population distance to 300 Mpc, in accordance with the advanced LIGO range for BNS systems. We find that essentially every realization peaks at least 1 mag brighter than even the shallower detection threshold (Fig. 5), and hence we conclude that Rubin will be capable of finding all EM counterparts to BNS GW triggers if it responds to them within a few days. However, like in the NSBH case, we neglect line-of-sight extinction and the observing cadence, defining detections only by the brightness of the realization relative to the detectability threshold. We note that the brightness of EM counterparts (and hence their detectability) may be enhanced by gravitational lensing. Evidence of this may manifest in the GW signals, in particular in candidate ‘mass gap’ mergers where one (or both) binary constituents are placed in the range $3\text{--}5 M_{\odot}$ in low latency (Smith et al. 2023).

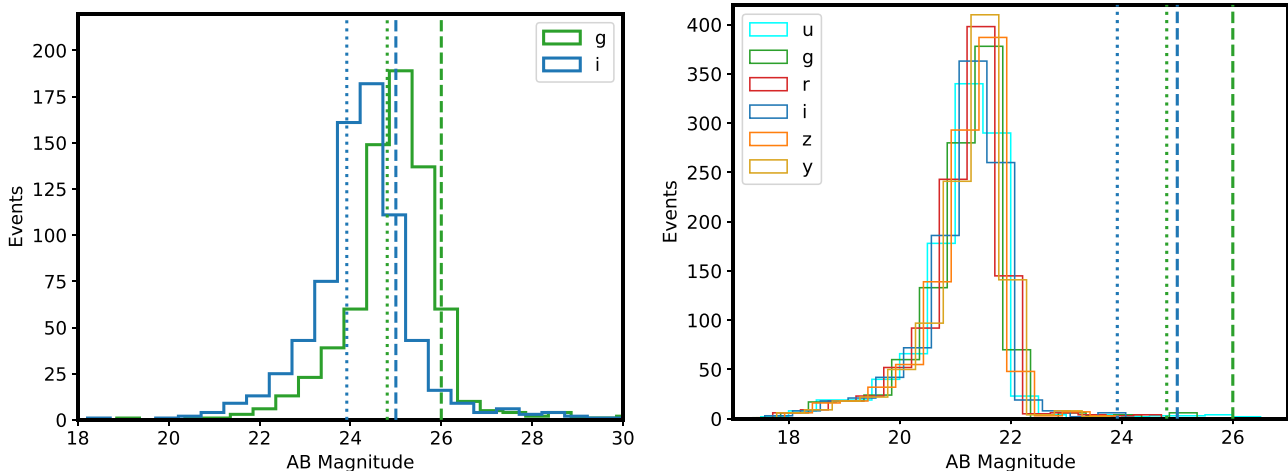


Figure 5. Histograms of the peak kilonova magnitude of 2000 realizations from our NSBH model (left) and the BNS model of Nicholl et al. (2021; right) in different photometric filters. The dotted lines show the single visit LSST WFD survey limits (Ivezić et al. 2019) for the *g* and *i* bands, and the GW follow-up limits (Andreoni et al. 2022) are shown by the dashed lines.

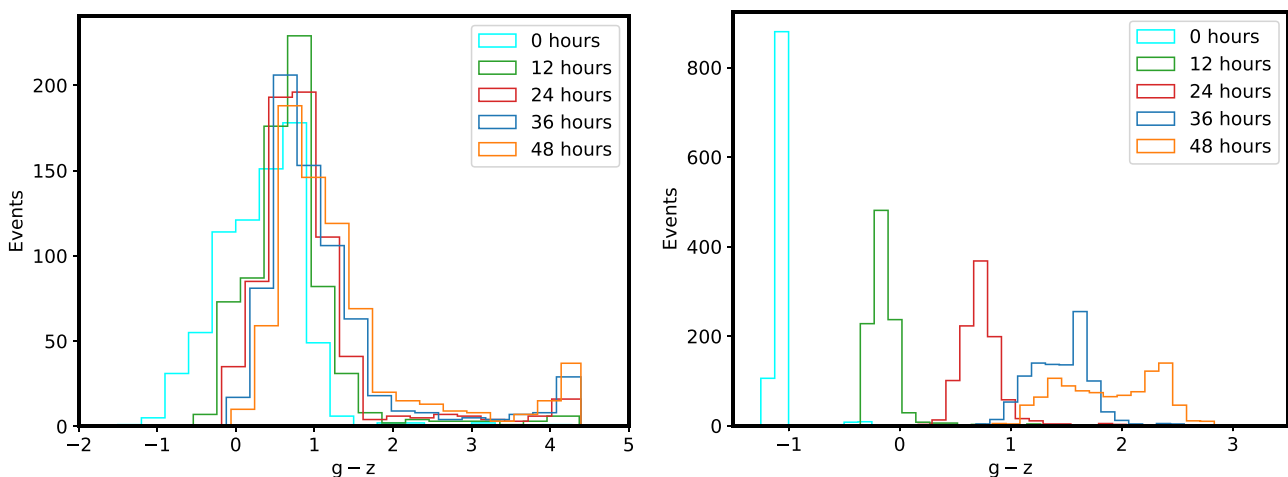


Figure 6. The colour evolution of NSBH kilonovae (left) and BNS kilonovae (right). The histograms show the distribution of *g*–*z* colours for the simulated populations at time intervals of 12 h following the merger. Due to the relative paucity of blue emission, the NSBH model predicts very little colour evolution and a consistently red transient. By contrast, the BNS model predicts rapid blue-to-red evolution over the first 2 d.

In Fig. 6, we show the expected colour evolution of the NSBH and BNS kilonovae. Notably, the NSBH kilonovae show little colour evolution, with a consistent *g*–*z* colour distribution centred around 1. Conversely, the BNS kilonovae are seen to evolve rapidly in colour over the first 2 d, becoming comparable to the NSBH kilonovae after ~ 24 h. This is likely a product of the lack of ‘blue’ emission from NSBH mergers, and reinforces the need for early observations to distinguish between the two in cases where the GW signal can not.

6 CONCLUSIONS

We present a new semi-analytic framework capable of predicting NSBH kilonova light curves from input binary properties. The model is integrated into the MOSFIT platform, and can be used for fast generation of libraries of light curves from an input binary population, predicting EM signals accompanying NSBH GW mergers, or performing multimessenger parameter inference from GW–EM data sets.

We demonstrate that a fiducial NSBH binary with $M_{\text{BH}} = 5$ and $M_{\text{NS}} = 1.4 M_{\odot}$ is broadly consistent with existing candidate kilonova counterparts to cosmological SGRBs with only minor tuning of parameters. However, we also demonstrate that NSBH systems are not capable of producing ‘blue’ emission (likely from lanthanide-poor ejecta) in quantities sufficient to match the light curve of GW 170817 unless other processes like shock heating from a GRB jet are included. Simulations (e.g. Fernández et al. 2019) suggest that material may be present in polar regions at the time of jet launch, but it is unclear whether there is sufficient mass to result in a signal similar to the one proposed by Piro & Kollmeier (2018). Our model indicates that for our assumed prior distributions, less than a third of NSBH mergers within the LIGO range of ~ 600 Mpc will have EM counterparts detectable with Rubin/LSST, even before accounting for survey cadence and line-of-sight extinction.

Our modelling suggests that early ($\lesssim 2$ d) observations of emergent kilonovae will be essential to distinguish BNS and NSBH mergers in cases where GW signals are absent or ambiguous. We also show

that NSBH kilonovae may not peak at optical frequencies until up to a week after merger for certain viewing angles. The first discovery of an EM signal from an NSBH merger remains a key objective of GW–EM and transient astronomy. Its identification will serve to validate (or iterate) merger models, as was done for the BNS case following GW 170817. Our model provides an early framework for interpreting the emission from such a system, and a platform for further development following observational ratification.

ACKNOWLEDGEMENTS

We are extremely grateful to Rodrigo Fernandez for fruitful discussions that helped shape the model. We thank the anonymous referee for their constructive comments that improved the quality of the manuscript.

MN and BG acknowledge funding by the European Research Council (ERC) under the European Union’s Horizon 2020 research and innovation programme (grant agreement number 948381). GPS acknowledges support from The Royal Society, the Leverhulme Trust, and the Science and Technology Facilities Council (grant numbers ST/N021702/1 and ST/S006141/1).

DATA AVAILABILITY

The model is available as part of MOSFIT v1.1.9, and can be accessed at <https://github.com/guillochon/MOSFIT>. Installation and general usage instructions are available at <http://mosfit.readthedocs.io/>.

REFERENCES

- Abbott B. P. et al., 2016, *Phys. Rev. Lett.*, 116, 061102
 Abbott B. P. et al., 2017a, *Phys. Rev. Lett.*, 119, 161101
 Abbott B. P. et al., 2017b, *ApJ*, 848, L12
 Abbott B. P. et al., 2020, *Living Rev. Relativ.*, 23, 3
 Abbott R. et al., 2021a, *Phys. Rev. X*, 11, 021053
 Abbott R. et al., 2021b, *ApJ*, 913, L7
 Abbott R. et al., 2021c, *ApJ*, 915, L5
 Acernese F. et al., 2015, *J. Phys. Conf. Ser.*, 610, 012014
 Andreoni I. et al., 2017, *PASA*, 34, e069
 Andreoni I. et al., 2022, *ApJS*, 260, 18
 Arcavi I., 2018, *ApJ*, 855, L23
 Arcavi I. et al., 2017, *ApJ*, 848, L33
 Arnett W. D., 1982, *ApJ*, 253, 785
 Ascenzi S. et al., 2019, *MNRAS*, 486, 672
 Barbieri C., Salafia O. S., Perego A., Colpi M., Ghirlanda G., 2019, *A&A*, 625, A152
 Bardeen J. M., Press W. H., Teukolsky S. A., 1972, *ApJ*, 178, 347
 Barnes J., Kasen D., 2013, *ApJ*, 775, 18
 Barnes J., Kasen D., Wu M.-R., Martínez-Pinedo G., 2016, *ApJ*, 829, 110
 Barthelmy S. D. et al., 2005, *Space Sci. Rev.*, 120, 143
 Belczynski K. et al., 2020, *A&A*, 636, A104
 Berger E., 2014, *ARA&A*, 52, 43
 Berger E., Fong W., Chornock R., 2013, *ApJ*, 774, L23
 Binnington T., Poisson E., 2009, *Phys. Rev. D*, 80, 084018
 Brege W. et al., 2018, *Phys. Rev. D*, 98, 063009
 Breschi M., Perego A., Bernuzzi S., Del Pozzo W., Nedora V., Radice D., Vescovi D., 2021, *MNRAS*, 505, 1661
 Broekgaarden F. S., Berger E., 2021, *ApJ*, 920, L13
 Broekgaarden F. S. et al., 2021, *MNRAS*, 508, 5028
 Bulla M., 2019, *MNRAS*, 489, 5037
 Bulla M., 2023, *MNRAS*, 520, 2558
 Chen H.-Y., Vitale S., Foucart F., 2021, *ApJ*, 920, L3
 Chornock R. et al., 2017, *ApJ*, 848, L19
 Christie I. M., Lalakos A., Tchekhovskoy A., Fernández R., Foucart F., Quataert E., Kasen D., 2019, *MNRAS*, 490, 4811
 Cobb B. E., Bailyn C. D., van Dokkum P. G., Natarajan P., 2006, *ApJ*, 651, L85
 Coughlin M. W., Dietrich T., 2019, *Phys. Rev. D*, 100, 043011
 Coughlin M. W., Dietrich T., Margalit B., Metzger B. D., 2019, *MNRAS*, 489, L91
 Coulter D. A. et al., 2017, *Science*, 358, 1556
 Covino S. et al., 2006, *A&A*, 447, L5
 Cowperthwaite P. S. et al., 2017, *ApJ*, 848, L17
 Cucchiara A. et al., 2013, *ApJ*, 777, 94
 D’Avanzo P. et al., 2018, *A&A*, 613, L1
 Damour T., Nagar A., 2009, *Phys. Rev. D*, 80, 084035
 Darbha S., Kasen D., 2020, *ApJ*, 897, 150
 Della Valle M. et al., 2006, *Nature*, 444, 1050
 Desai D., Metzger B. D., Foucart F., 2019, *MNRAS*, 485, 4404
 Dichiaro S. et al., 2021, *ApJ*, 923, L32
 Dietrich T., Coughlin M. W., Pang P. T. H., Bulla M., Heinzel J., Issa L., Tews I., Antier S., 2020, *Science*, 370, 1450
 Drout M. R. et al., 2017, *Science*, 358, 1570
 Eichler D., Livio M., Piran T., Schramm D. N., 1989, *Nature*, 340, 126
 Eldridge J. J., Stanway E. R., Tang P. N., 2019, *MNRAS*, 482, 870
 Etienne Z. B., Liu Y. T., Shapiro S. L., Baumgarte T. W., 2009, *Phys. Rev. D*, 79, 044024
 Evans P. A. et al., 2017, *Science*, 358, 1565
 Eyles R. A. J. et al., 2019, *MNRAS*, 489, 13
 Farrow N., Zhu X.-J., Thrane E., 2019, *ApJ*, 876, 18
 Fernández R., Metzger B. D., 2013, *MNRAS*, 435, 502
 Fernández R., Kasen D., Metzger B. D., Quataert E., 2015, *MNRAS*, 446, 750
 Fernández R., Tchekhovskoy A., Quataert E., Foucart F., Kasen D., 2019, *MNRAS*, 482, 3373
 Fernández R., Foucart F., Lippuner J., 2020, *MNRAS*, 497, 3221
 Flanagan É. É., Hinderer T., 2008, *Phys. Rev. D*, 77, 021502
 Fong W., Berger E., Margutti R., Zauderer B. A., 2015, *ApJ*, 815, 102
 Fong W. et al., 2021, *ApJ*, 906, 127
 Foreman-Mackey D., Hogg D. W., Lang D., Goodman J., 2013, *PASP*, 125, 306
 Foucart F., Duez M. D., Kidder L. E., Teukolsky S. A., 2011, *Phys. Rev. D*, 83, 024005
 Foucart F., Duez M. D., Kidder L. E., Scheel M. A., Szilagy B., Teukolsky S. A., 2012, *Phys. Rev. D*, 85, 044015
 Foucart F. et al., 2013, *Phys. Rev. D*, 87, 084006
 Foucart F. et al., 2014, *Phys. Rev. D*, 90, 024026
 Foucart F. et al., 2015, *Phys. Rev. D*, 91, 124021
 Foucart F., Hinderer T., Nisanke S., 2018, *Phys. Rev. D*, 98, 081501
 Foucart F., Duez M. D., Kidder L. E., Nisanke S. M., Pfeiffer H. P., Scheel M. A., 2019, *Phys. Rev. D*, 99, 103025
 Fox D. B. et al., 2005, *Nature*, 437, 845
 Fragione G., 2021, *ApJ*, 923, L2
 Freiburghaus C., Rosswog S., Thielemann F.-K., 1999, *ApJ*, 525, L121
 Fujibayashi S., Shibata M., Wanajo S., Kiuchi K., Kyutoku K., Sekiguchi Y., 2020, *Phys. Rev. D*, 101, 083029
 Fuller J., Ma L., 2019, *ApJ*, 881, L1
 Fynbo J. P. U. et al., 2006, *Nature*, 444, 1047
 Gal-Yam A. et al., 2006, *Nature*, 444, 1053
 Gao H., Lei W.-H., Zhu Z.-P., 2022, *ApJ*, 934, L12
 Gehrels N. et al., 2004, *ApJ*, 611, 1005
 Gehrels N. et al., 2006, *Nature*, 444, 1044
 Gillanders J. H., Smartt S. J., Sim S. A., Bauswein A., Goriely S., 2022, *MNRAS*, 515, 631
 Gillanders J. H., Sim S. A., Smartt S. J., Goriely S., Bauswein A., 2023a, preprint (arXiv:2306.15055)
 Gillanders J. H. et al., 2023b, preprint (arXiv:2308.00633)
 Goldstein A. et al., 2017, *ApJ*, 848, L14
 Gompertz B. P., O’Brien P. T., Wynn G. A., Rowlinson A., 2013, *MNRAS*, 431, 1745
 Gompertz B. P. et al., 2018, *ApJ*, 860, 62
 Gompertz B. P., Levan A. J., Tanvir N. R., 2020, *ApJ*, 895, 58

- Gompertz B. P., Nicholl M., Schmidt P., Pratten G., Vecchio A., 2022, *MNRAS*, 511, 1454
- Gompertz B. P. et al., 2023, *Nat. Astron.*, 7, 67
- Guillochon J., Nicholl M., Villar V. A., Mockler B., Narayan G., Mandel K. S., Berger E., Williams P. K. G., 2018, *ApJS*, 236, 6
- Hallinan G. et al., 2017, *Science*, 358, 1579
- Hinderer T., 2008, *ApJ*, 677, 1216
- Hinderer T., Lackey B. D., Lang R. N., Read J. S., 2010, *Phys. Rev. D*, 81, 123016
- Hjorth J. et al., 2005, *Nature*, 437, 859
- Hotokezaka K., Tanaka M., Kato D., Gaigalas G., 2023, *MNRAS*, 526, L155
- Ivezić Ž. et al., 2019, *ApJ*, 873, 111
- Jin Z.-P., Li X., Cano Z., Covino S., Fan Y.-Z., Wei D.-M., 2015, *ApJ*, 811, L22
- Jin Z.-P. et al., 2016, *Nat. Commun.*, 7, 12898
- Jin Z.-P. et al., 2018, *ApJ*, 857, 128
- Jin Z.-P., Covino S., Liao N.-H., Li X., D’Avanzo P., Fan Y.-Z., Wei D.-M., 2020, *Nat. Astron.*, 4, 77
- Just O., Bauswein A., Ardevol Pulpillo R., Goriely S., Janka H. T., 2015, *MNRAS*, 448, 541
- Just O., Kullmann I., Goriely S., Bauswein A., Janka H. T., Collins C. E., 2022, *MNRAS*, 510, 2820
- Kagra Collaboration, 2019, *Nat. Astron.*, 3, 35
- Kasen D., Metzger B., Barnes J., Quataert E., Ramirez-Ruiz E., 2017, *Nature*, 551, 80
- Kasliwal M. M. et al., 2017a, *Science*, 358, 1559
- Kasliwal M. M., Korobkin O., Lau R. M., Wollaeger R., Fryer C. L., 2017b, *ApJ*, 843, L34
- Kawaguchi K., Kyutoku K., Nakano H., Okawa H., Shibata M., Taniguchi K., 2015, *Phys. Rev. D*, 92, 024014
- Kawaguchi K., Kyutoku K., Shibata M., Tanaka M., 2016, *ApJ*, 825, 52
- Kawaguchi K., Shibata M., Tanaka M., 2020, *ApJ*, 889, 171
- Klion H., Duffell P. C., Kasen D., Quataert E., 2021, *MNRAS*, 502, 865
- Korobkin O., Rosswog S., Arcones A., Winteler C., 2012, *MNRAS*, 426, 1940
- Korobkin O. et al., 2021, *ApJ*, 910, 116
- Kouveliotou C., Meegan C. A., Fishman G. J., Bhat N. P., Briggs M. S., Koshut T. M., Paciesas W. S., Pendleton G. N., 1993, *ApJ*, 413, L101
- Krüger C. J., Foucart F., 2020, *Phys. Rev. D*, 101, 103002
- Kyutoku K., Okawa H., Shibata M., Taniguchi K., 2011, *Phys. Rev. D*, 84, 064018
- Kyutoku K., Ioka K., Okawa H., Shibata M., Taniguchi K., 2015, *Phys. Rev. D*, 92, 044028
- Kyutoku K., Kiuchi K., Sekiguchi Y., Shibata M., Taniguchi K., 2018, *Phys. Rev. D*, 97, 023009
- LIGO Scientific Collaboration, 2015, *Class. Quant. Grav.*, 32, 074001
- Lamb D. Q. et al., 2000, in Holt S. S., Zhang W. W., eds, *AIP Conf. Ser. Vol. 522, Cosmic Explosions: Tenth Astrophysics Conference*. p. 265
- Lamb G. P. et al., 2019a, *ApJ*, 870, L15
- Lamb G. P. et al., 2019b, *ApJ*, 883, 48
- Lattimer J. M., Prakash M., 2001, *ApJ*, 550, 426
- Lattimer J. M., Schramm D. N., 1974, *ApJ*, 192, L145
- Levan A. et al., 2023, preprint (arXiv:2307.02098)
- Li L.-X., Paczyński B., 1998, *ApJ*, 507, L59
- Lien A. et al., 2016, *ApJ*, 829, 7
- Lipunov V. M. et al., 2017, *ApJ*, 850, L1
- Lovelace G., Duez M. D., Foucart F., Kidder L. E., Pfeiffer H. P., Scheel M. A., Szilágyi B., 2013, *Class. Quant. Grav.*, 30, 135004
- Lyman J. D. et al., 2018, *Nat. Astron.*, 2, 751
- Mandel I., Smith R. J. E., 2021, *ApJ*, 922, L14
- Mangano V. et al., 2007, *A&A*, 470, 105
- Mapelli M., Giacobbo N., 2018, *MNRAS*, 479, 4391
- Margalit B., Metzger B. D., 2017, *ApJ*, 850, L19
- Margalit B., Metzger B. D., 2019, *ApJ*, 880, L15
- Margutti R. et al., 2017, *ApJ*, 848, L20
- Margutti R. et al., 2018, *ApJ*, 856, L18
- McCully C. et al., 2017, *ApJ*, 848, L32
- Meegan C. et al., 2009, *ApJ*, 702, 791
- Mei A. et al., 2022, *Nature*, 612, 236
- Metzger B. D., 2019, *Living Rev. Relativ.*, 23, 1
- Metzger B. D., Fernández R., 2014, *MNRAS*, 441, 3444
- Metzger B. D. et al., 2010, *MNRAS*, 406, 2650
- Mooley K. P. et al., 2018, *Nature*, 554, 207
- Nativi L., Bulla M., Rosswog S., Lundman C., Kowal G., Gizzi D., Lamb G. P., Perego A., 2021, *MNRAS*, 500, 1772
- Nicholl M. et al., 2017a, *ApJ*, 848, L18
- Nicholl M., Guillochon J., Berger E., 2017b, *ApJ*, 850, 55
- Nicholl M., Margalit B., Schmidt P., Smith G. P., Ridley E. J., Nuttall J., 2021, *MNRAS*, 505, 3016
- Norris J. P., Bonnell J. T., 2006, *ApJ*, 643, 266
- Norris J. P., Gehrels N., Scargle J. D., 2010, *ApJ*, 717, 411
- O’Connor B. et al., 2021, *MNRAS*, 502, 1279
- Paczynski B., 1986, *ApJ*, 308, L43
- Pannarale F., Ohme F., 2014, *ApJ*, 791, L7
- Paschalidis V., Ruiz M., Shapiro S. L., 2015, *ApJ*, 806, L14
- Pian E. et al., 2017, *Nature*, 551, 67
- Piro A. L., Kollmeier J. A., 2018, *ApJ*, 855, 103
- Postnikov S., Prakash M., Lattimer J. M., 2010, *Phys. Rev. D*, 82, 024016
- Qin Y., Fragos T., Meynet G., Andrews J., Sørensen M., Song H. F., 2018, *A&A*, 616, A28
- Raaijmakers G. et al., 2021, *ApJ*, 922, 269
- Raitel C. A., Özel F., Psaltis D., 2018, *ApJ*, 857, L23
- Rastinejad J. C. et al., 2021, *ApJ*, 916, 89
- Rastinejad J. C. et al., 2022, *Nature*, 612, 223
- Rosswog S., 2005, *ApJ*, 634, 1202
- Rosswog S., Sollerman J., Feidt U., Goobar A., Korobkin O., Wollaeger R., Fremling C., Kasliwal M. M., 2018, *A&A*, 615, A132
- Savchenko V. et al., 2017, *ApJ*, 848, L15
- Shapiro S. L., Teukolsky S. A., 1986, *Black Holes, White Dwarfs and Neutron Stars: The Physics of Compact Objects*. Wiley, New York
- Shappee B. J. et al., 2017, *Science*, 358, 1574
- Siegel D. M., Metzger B. D., 2017, *Phys. Rev. Lett.*, 119, 231102
- Siegel D. M., Metzger B. D., 2018, *ApJ*, 858, 52
- Smartt S. J. et al., 2017, *Nature*, 551, 75
- Smith G. P. et al., 2023, *MNRAS*, 520, 702
- Soares-Santos M. et al., 2017, *ApJ*, 848, L16
- Stamatikos M. et al., 2021, *GRB Coordinates Network*, 31209, 1
- Steinle N., Kesden M., 2021, *Phys. Rev. D*, 103, 063032
- Steinle N., Gompertz B. P., Nicholl M., 2023, *MNRAS*, 519, 891
- Tanaka M., Hotokezaka K., 2013, *ApJ*, 775, 113
- Tanaka M., Hotokezaka K., Kyutoku K., Wanajo S., Kiuchi K., Sekiguchi Y., Shibata M., 2014, *ApJ*, 780, 31
- Tanaka M., Kato D., Gaigalas G., Kawaguchi K., 2020, *MNRAS*, 496, 1369
- Tanvir N. R., Levan A. J., Fruchter A. S., Hjorth J., Hounsell R. A., Wiersema K., Tunnicliffe R. L., 2013, *Nature*, 500, 547
- Tanvir N. R. et al., 2017, *ApJ*, 848, L27
- The LIGO Scientific Collaboration, 2021a, preprint (arXiv:2108.01045)
- The LIGO Scientific Collaboration, 2021b, preprint (arXiv:2111.03606)
- Thone C. C., de Ugarte Postigo A., Gorosabel J., Tanvir N., Fynbo J. P. U., 2013, *GRB Coordinates Network*, 14744, 1
- Troja E., King A. R., O’Brien P. T., Lyons N., Cusumano G., 2008, *MNRAS*, 385, L10
- Troja E. et al., 2017, *Nature*, 551, 71
- Troja E. et al., 2018a, *Nat. Commun.*, 9, 4089
- Troja E. et al., 2018b, *MNRAS*, 478, L18
- Troja E. et al., 2019, *MNRAS*, 489, 2104
- Troja E. et al., 2022, *Nature*, 612, 228
- Utsumi Y. et al., 2017, *PASJ*, 69, 101
- Valenti S. et al., 2017, *ApJ*, 848, L24
- Villar V. A. et al., 2017, *ApJ*, 851, L21
- Villasenor J. S. et al., 2005, *Nature*, 437, 855
- Wade L., Creighton J. D. E., Ochsner E., Lackey B. D., Farr B. F., Littenberg T. B., Raymond V., 2014, *Phys. Rev. D*, 89, 103012
- Watson D. et al., 2019, *Nature*, 574, 497
- Xiao S. et al., 2022, preprint (arXiv:2205.02186)
- Yagi K., Yunes N., 2017, *Phys. Rep.*, 681, 1

Yang B. et al., 2015, *Nat. Commun.*, 6, 7323

Yang J. et al., 2022, *Nature*, 612, 232

Zhu J.-P., Yang Y.-P., Liu L.-D., Huang Y., Zhang B., Li Z., Yu Y.-W., Gao H., 2020, *ApJ*, 897, 20

Zhu J.-P., Wu S., Yang Y.-P., Zhang B., Yu Y.-W., Gao H., Cao Z., Liu L.-D., 2021, *ApJ*, 921, 156

Zhu J.-P., Wang X. I., Sun H., Yang Y.-P., Li Z., Hu R.-C., Qin Y., Wu S., 2022, *ApJ*, 936, L10

This paper has been typeset from a $\text{\TeX}/\text{\LaTeX}$ file prepared by the author.